Nanoscale Horizons

ROYAL SOCIETY OF CHEMISTRY

COMMUNICATION

View Article Online
View Journal | View Issue

Check for updates

Cite this: *Nanoscale Horiz.*, 2025, **10**, 3013

Received 30th April 2025,
Accepted 14th August 2025

DOI: 10.1039/d5nh00290g

rsc.li/nanoscale-horizons

Published on 15 August 2025. Downloaded on 2/6/2026 8:16:01 PM.

Nanostructured $LiNi_{0.80}Co_{0.15}Al_{0.05}O_2$ (NCA) for fast-charging, high-capacity battery cathodes

Victoria M. Basile,[a] Chun-Han Lai,[b] Grace Y. Kim,[a] Christopher S. Choi,[b] Danielle M. Butts,[b] Kodi Thurber,[a] Sophia C. King[a] and Sarah H. Tolbert *[abc]

Nanostructuring, which shortens lithium-ion diffusion lengths, can help facilitate pseudocapacitive behavior in some battery materials. Here, nanostructured $LiNi_{0.80}Co_{0.15}Al_{0.05}O_2$ (NCA), with porosity and decreased crystallite size compared to commercial bulk NCA, was synthesized using a colloidal polymer template. Small particles (~150 nm) were obtained using rapid thermal annealing (RTA), while medium particles (~300 nm) were obtained with conventional heating. X-ray photoelectron spectroscopy (XPS) was used to quantify surface Li_2CO_3 and NiO-like contaminants, which hinder lithium-ion diffusion, especially at fast rates. Electrochemical kinetics studies were used to quantify the benefits associated with nanostructuring. While all nanostructured samples displayed faster charge/discharge kinetics compared to the bulk materials, NCA with medium particle sizes showed the highest specific capacity at the fast rates (150 mAh g^{-1} at 16C). To explore full-cell behavior, nanostructured NCA was paired with a pseudocapacitive anode, achieving 95 W h kg^{-1} energy density at a current density of 1260 W kg^{-1} and stable cycling for 2000 cycles at 10C.

[a] *Department of Chemistry and Biochemistry, University of California, Los Angeles, California 90095, USA. E-mail: tolbert@chem.ucla.edu*
[b] *Department of Materials Science and Engineering, University of California, Los Angeles, California 90095, USA*
[c] *The California NanoSystems Institute, University of California, Los Angeles, California 90095, USA*

Sarah H. Tolbert

I joined the Editorial Board of Nanoscale Horizons in 2017, when the journal was in its infancy. It was a real challenge to figure out how to turn a new journal into a top journal, but it has been a true pleasure to see the progress and to watch the journal grow and flourish. As a professor in both Chemistry and Materials Science who works in fields ranging from energy storage to plastic electronics and from superhard materials to nanomagnetics, I know how important it is to find a cross disciplinary platform that can allow researchers to share advances with people outside of their specialty. Nanoscale Horizons is one of those unique journals that strives to make connections. Happy tenth anniversary Nanoscale Horizons – you are a credit to the fantastically interdisciplinary field of nanoscience!

New concepts

As the electrification of our society grows, the need for fast-charging electrical energy storage solutions also increases. Lithium-ion batteries currently offer the fastest charging times, but increased charging speed without significantly compromising capacity would enable new technologies. Nanostructuring of electrode materials can be used to reduce lithium-ion diffusion distances and thus to increase charge/discharge speed, and this has been applied to both anode materials and to phosphate cathodes. However, the most common lithium-ion cathodes the layered oxide, have proven difficult to create with good performance in nanoscale form because of their highly reactive surfaces and tendency for cation disorder. In this work, we show that the fast-charging layered cathode $LiNi_{0.80}Co_{0.15}Al_{0.05}O_2$ (NCA) can be created as a nanoporous material with low cation disorder using polymer templating. By optimizing grain size, surface chemistry, and electrode architecture, fast-charging electrodes can be produced. Interestingly, the smallest grain materials do not show the best performance. Instead, medium-size nanoporous materials with reduced surface area show the highest capacity retention at high charge/discharge rate, the lowest overpotentials, and the most signatures of pseudocapacitive behavior. When paired with a pseudocapactive anode, fast-charging full-cells with good cycle stability can be created, demonstrating the practical potential of these materials.

Introduction

As the popularity of electric vehicles (EVs) rises, fast-charging lithium-ion batteries are key for large-scale implementation.[1,2] Charging times on the order of minutes, instead of hours, are required to be comparable to internal combustion engine

Published on 15 August 2025. Downloaded on 2/6/2026 8:16:01 PM.

fueling times. Short charging times can be accomplished with supercapacitors,[3] but the range of supercapacitor EVs is limited to less than 20 miles.[4,5] Lithium-ion batteries are currently the standard for higher capacity needs, but the long charging time and high cost of current batteries leave room for improvement.[6] One solution to designing fast charging cathode materials, while still retaining high driving range, is the use of lithium-ion batteries with shortened lithium-ion diffusion lengths through nanostructuring.[7] This has been effectively employed in lithium iron phosphate (LFP) batteries to increase power density, producing some of the most promising advances in low-cost, faster-charging batteries. The low voltage of LFP based batteries, however, limits the energy density, leaving room for systems that can combine high-energy and high-power density through nanostructuring.[8–10]

Materials can be nanostructured using many techniques such as nanoparticle synthesis/assembly, hydrothermal synthesis, or electrodeposition.[11] One relatively simple technique, which results in high surface area as well as homogeneous nanoscale porosity, is sol–gel synthesis combined with colloidal polymer templates such as poly(methyl methacrylate) (PMMA).[12] Although the colloidal template is easily removed by moderate heating to leave a nanoporous structure, high crystallization temperatures (>700 °C) are required for many battery materials, which can diminish the desired nanostructure. Generally, conventional slow heating promotes grain growth, while rapid thermal annealing (RTA) can support smaller particle sizes.[13]

Nanostructured battery materials allow for the reduction of lithium-ion diffusion lengths so that slow solid-state diffusion is no longer rate limiting and fast charging can be achieved. This process, where pseudocapacitive characteristics emerge as a result of nanostructuring, has been termed 'extrinsic pseudocapacitance'. One of the best examples of this phenomenon is with the well-known cathode material, $LiCoO_2$.[14] Even though the material in bulk form does not exhibit pseudocapacitive properties, when reduced to dimensions ~6 nm, galvanostatic experiments lead to a linear dQ/dV, indicative of a capacitive response. Similar examples of extrinsic pseudocapacitance have been seen in many nanostructured materials with medium voltage ranges, such as MoO_2,[15–17] MoS_2,[18–23] and TiO_2.[24–27] In some of these materials, the key to the development of pseudocapacitive properties is suppression of bulk intercalation induced phase transitions at small size.[15,16,24,28,29] Pseudocapacitive behavior has generated considerable interest, especially for EVs, because it allows for the desirable combination of fast-charging and reasonable driving range. A variety of electrochemical measurement methods have been developed to identify signatures of pseudocapacitive charge storage.[26,30–34]

While there are several examples of pseudocapacitive materials that operate in a 'medium' potential range below 2.5 V *vs.* Li/Li^+, there are fewer examples of pseudocapacitive materials operating at high-voltage. One known pseudocapacitive material operating in the 3.4–4.5 voltage range (*vs.* Li/Li^+) is nanostructured $LiMn_2O_4$, but it suffers from low capacity that is further reduced by an inactive surface in nanostructured form.[35–37] For practical fast-charging energy storage devices, pseudocapacitive cathodes with higher capacity are needed.

One cathode material for lithium-ion batteries that has generated considerable interest because of its high specific capacity and intrinsically fast charging capabilities is $LiNi_{0.80}Co_{0.15}Al_{0.05}O_2$ (NCA), a layered transition metal oxide.[38,39] Layered transition metal oxide cathodes, including NCA and $LiNi_xMn_yCo_zO_2$ (NMC) materials with various stoichiometries, are considered the most viable of the current higher voltage cathode materials.[40] These materials utilize a mixture of metals to frustrate the phase transitions that occur in pure $LiCoO_2$ or $LiNiO_2$, resulting in more stable and faster cycling capabilities. Systems high in Ni, like NCA and high Ni NMC, further have the highest capacities, though this is accompanied by reduced chemical stability.[41,42] Of all of these related materials, NCA shows the fast rate capabilities in bulk form, largely due to the stabilizing effects of the cobalt and aluminum dopants, which both suppress phase transitions and facilitate Li diffusion channels.[43–48] For this reason, we chose NCA as the most interesting candidate to explore in nanostructured form to produce a high-rate cathode material through extrinsic pseudocapacitance. Importantly, since nanostructuring in NCA is only necessary to decrease diffusion lengths and not to suppress phase transitions, pseudocapacitive behavior may begin to develop at larger sizes.

Despite its promise, NCA also has a number of drawbacks. NCA of all sizes suffers from cation mixing, which occurs when partly-reduced Ni^{2+} present in the transition-metal-oxide layers migrates to the Li^+ layer due to their similar ionic sizes.[49] This leads to local shrinkage of the lithium diffusion pathways during cycling and decreased electrochemical performance.[50] In order to mitigate the effect of cation mixing, high calcination temperatures (which are not ideal for maintaining nanoscale structure) under oxygen flow are required to promote the oxidation of Ni^{2+} to Ni^{3+}.[51] The degree of cation mixing is easily determined using X-ray diffraction (XRD) by examining the integrated intensity ratio of the (003) to (104) diffraction peaks. Previous studies have determined that a $I(003)/I(104)$ ratio above 1.2 is necessary for optimal electrochemical performance.[52]

It is also well known that NCA is sensitive to CO_2 and water in the air, which react with excess lithium on the surface and near-surface lithium to form an insulating Li_2CO_3 layer.[53,54] The removal of lattice-lithium near the surface, combined with reduction of near-surface nickel, can further result in the formation of an electrochemically inactive rock-salt (NiO-like) layer beneath the Li_2CO_3.[55–57] Both the Li_2CO_3 and NiO-like layers can hinder lithium-ion diffusion, especially at high rates.[53] Unfortunately, nanostructured NCA, with decreased particle sizes, should have increased sensitivity to air. As a result, all nanostructured NCA materials in this work were kept air-free.

Another component for our fast-charging cathode is an optimized binder. Recently, conductive polymers, such as poly(3-hexylthiophene-2,5-diyl) (P3HT),[58] poly(3,4-ethylenedioxythiophene):poly(styrenesulfonate) (PEDOT:PSS),[59] and polypyrrole (PPy),[60] have been used as conductive binders for battery electrodes due to their high electronic and ionic conductivity compared to traditional insulating binders, such as polyvinylidene fluoride (PVDF). P3HT, in particular, has shown promise

 This journal is © The Royal Society of Chemistry 2025

Published on 15 August 2025. Downloaded on 2/6/2026 8:16:01 PM.

as a conductive binder for NCA cathodes that helped suppress electrolyte breakdown at the NCA surface.[58] P3HT, which has been widely studied for use in organic photovoltaics,[61] is electrochemically doped in the operational voltage window of NCA (2.7–4.2 V), facilitating electronic/ionic conductivity and thus high-rate charge storage.[58] Thus, P3HT was used as the binder in our system to facilitate high-rate charging and discharging.

Finally, we consider recent work on layered metal oxide cathodes with nanoscale dimensions. While there exist layered transition metal oxide cathodes with varied morphologies, many show rather ordinary rate capabilities that would not be applicable for fast charging batteries. For example, a nickel-rich cathode $LiNi_{0.6}Co_{0.2}Mn_{0.2}O_2$, with a unique nano-brick morphology was found to exhibit a high, reversible capacity of 180.6 mAh g^{-1} at 0.1C, but its capacity falls to 98.6 mAh g^{-1} at 10C.[62] Similarly, a comparative analysis from of $LiNi_{0.83}Co_{0.12}Mn_{0.05-x}Al_xO_2$ (x = 0 [NMC], 0.025 [NMCA], or 0.05 [NCA]) in nanoparticle and nanofiber microstructural forms found the nanofibers to have higher capacities, but the maximum capacity at 10C was 27 mAh g^{-1}, 39 mAh g^{-1}, and 54 mAh g^{-1}, for each of the samples, respectively.[63] Work on $LiNi_{0.8}Co_{0.1}Mn_{0.1}O_2$ cathodes with nanosized primary particles using hollow micro-nano hierarchical microspheres achieved one of the higher capacities, retaining 144 mAh g^{-1} at 5C.[64] Other reported values for nanostructured NCA include nanoporous microspheres (151 mAh g^{-1} capacity at 2C),[65] microspheres with an isolated porous layer (190 mAh g^{-1} capacity at 2C),[66,67] nanocrystals (82 mAh g^{-1} capacity at 3C),[68] nanoplates (139 mAh g^{-1} capacity at 10C),[69,70] and holey 2D nanosheets, which show the most impressive rate behavior with 153 mAh g^{-1} capacity at 10C.[71] Unfortunately, none of these materials were cycled faster than 10C and no kinetic analyses were performed to identify their characteristic behavior.

In this letter, we thus present methods to synthesize porous nanostructured NCA with two different particle sizes. Electrochemical kinetics are used to examine high-rate performance and understand charge storage processes. We then paired the nanostructured NCA with a pseudocapacitive anode to test the high-rate performance and long-term cyclability in a full-cell as validation of practicability.

Experimental

Materials

The following chemicals were purchased and used as received: lithium nitrate (98 + %, MilliporeSigma), nickel nitrate hexahydrate (99.9985%, Alfa Aesar), cobalt nitrate hexahydrate (99 + %, Acros Organics), aluminum nitrate nonahydrate (98%, Alfa Aesar), triblock copolymer Pluronic F127 (EO100PO65EO100 M_W = 12600 Da, BASF), ammonium persulfate (98%, Alfa Aesar), ammonium lauryl sulfate (~30% in H_2O, Sigma Aldrich), methyl methacrylate (contains ≤30 ppm MEHQ as inhibitor, 99%, Sigma Aldrich), and hexanes (Fisher Chemical). Commercial bulk NCA was purchased from Quallion Corporation to use as a control. For electrode and coin cell assembly, the following chemicals were purchased and used as received: multi-walled carbon nanotubes (>95%, OD: 5–15 nm, US Research Nanomaterials, Inc.), carbon nanofibers ($D \times L$ 100 nm × 20–200 μm, Sigma-Aldrich), poly(3-hexylthiophene-2,5-diyl) (P3HT) (M_W 15 000–30 000, PDI = 1.6–1.8, regioregularity = 89–94%, Rieke Metals), *o*-xylenes (99%, Extra Dry, ACROS Organics), carbon black, Super P (Alfa Aesar), styrene-butadiene rubber (SBR, MTI corp.), carboxymethyl cellulose (CMC, MTI corp.), polyvinylidene fluoride (PVDF, Kynar), and *N*-methyl-2-pyrrolidone (NMP, Alfa Aesar).

Characterization

X-ray diffraction (XRD) was collected using a Bruker D8 Discover powder X-ray diffractometer using a Bragg–Brentano geometry. Scanning electron microscopy (SEM) images were obtained with a JOEL JSM-6700F field emission scanning electron microscope with 5 kV accelerating voltage. To examine the structure of the particles with transmission electron microscopy (TEM), we used an FEI Technai G2 TF20 high-resolution TEM, CryoEM and CryoET operating at an accelerating voltage of 200 kV with a TIETZ F415MP 16 megapixel 4k × 4k CCD detector. The powder was dispersed in NMP and deposited onto a copper TEM grid in the glove box; the grid was exposed to air for less than 30 seconds before analysis. Nitrogen porosimetry measurements were performed using either a Micromeritics TriStar II 3020 porosimeter or a Micromeritics ASAP 2020 Plus porosimeter. The adsorption branch of the isotherm was used to determine the surface area using the Brunauer–Emmett–Teller (BET) model. Volume weighted pore size distribution was determined from the adsorption isotherm using the Barrett–Joyner–Halenda (BJH) model with the Halsey equation and Faas correction. Surface sensitive elemental analysis was performed using X-ray photoelectron spectroscopy (XPS) using a Kratos Axis Ultra DLD spectrometer with a monochromatic Al Kα radiation source and a charge neutralizer filament to control charging of the sample. All spectra were calibrated to the advantageous carbon 1s peak at 284.8 eV. The air-free samples were transferred from a glovebox to the XPS sample chamber using an air-free sample transfer holder. The air-exposed samples were taken out of the glovebox and exposed to ambient air for 1 week before analysis. Argon ion etching was performed on select samples in the XPS chamber with a raster size of 2 mm×2 mm and an acceleration voltage of 4 kV for 30 seconds to 2 minutes.

Rietveld refinement using MAUD software

The XRD data were analyzed by Rietveld refinement using MAUD software. A $R\bar{3}m$ space group was used with Li^+/Ni^{2+} set at the 3a sites (0, 0, 0), $Li^+/Ni^{3+}/Co^{3+}/Al^{3+}$ at the 3b sites (0, 0, 0.5), and O at the 6c sites (0, 0, z_{ox}), where $z_{ox} \approx 0.250$ Å. The calculated pattern is evaluated with a weighted profile R factor (R_{wp}), where a R_{wp} less than 10% is considered a good fit. The refined c lattice parameter and value for z_{ox} were then used to calculate the slab (S) and interslab (I) thicknesses, where the interslab thickness is the thickness of the lithium-ion diffusion layer, using the following formulas:[72,73]

$$S = 2\left(\frac{1}{3} - z_{ox}\right)c \quad (1)$$

Published on 15 August 2025. Downloaded on 2/6/2026 8:16:01 PM.

$$I = \frac{c}{3} - S \quad (2)$$

Synthesis of the colloidal poly(methyl methacrylate) (PMMA) templates

The synthesis of the colloidal PMMA template is based on previous literature.[74,75] Deionized water (165 mL) was added to a three-neck round-bottom flask in an oil bath with a magnetic stirrer and a reflux condenser. The methyl methacrylate monomer (12.56 mL) was added dropwise to the flask. The solution was then heated from room temperature to 73 °C over 10 minutes. Once the reaction temperature exceeded 55 °C, the initiator, ammonium persulfate (0.08 g in 10 mL H_2O) was added dropwise. The reaction was then held at 73 °C for 3 hours. The resulting colloidal solution of PMMA was then extracted with hexanes in order to remove any unreacted monomer. SEM was used to determine the colloid size, which was 250 nm in diameter.

Synthesis of nanostructured $LiNi_{0.80}Co_{0.15}Al_{0.05}O_2$

Stoichiometric amounts of nickel nitrate hexahydrate, cobalt nitrate hexahydrate, and aluminum nitrate nonahydrate were dissolved in water, so that the total transition metal concentration (Ni + Co + Al) was 0.6 M. Lithium nitrate was also dissolved with 5% molar excess (Li : (Ni + Co + Al) = 1.05 : 1). Once completely dissolved, this solution was mixed with the colloidal 250 nm PMMA template (synthesis above) in a 1 : 1.5 vol ratio of the final NCA material to PMMA. This was followed by the addition of 3.8 wt% Pluronic F127 (with respect to colloidal PMMA) in order to stabilize the colloidal template in the salt solution. This solution was then stirred for 3 hours before it was poured into a Petri dish and dried in an 80 °C oven overnight. The resulting powder was heated in a tube furnace under flowing oxygen, first at 180 °C to drive out any remaining water and then at 450 °C to remove the template, leaving a nanostructured NCA precursor. The NCA precursor was then ground with a mortar and pestle before further heat treatment. Either a rapid thermal annealing (RTA) or a conventional heat treatment was used to obtain "PMMA/RTA" or "PMMA/no-RTA" samples, respectively. For PMMA/no-RTA the following heat treatment program was followed, all under flowing oxygen: a 1 hour ramp from room temperature to 800 °C, followed by 2 hours at 800 °C, then the oven was let naturally cool to 350 °C before the sample was taken directly into a glovebox while hot, to decrease exposure to water in the air. For the PMMA/RTA sample: the furnace was preheated to 850 °C, the sample was then added to the hot furnace and the oxygen flow was turned on. The sample was kept at 850 °C for 5 minutes, the furnace was then opened to allow for immediate cooling to 700 °C. The sample was held at 700 °C for 12 hours under oxygen flow, then cooled naturally to 350 °C to be directly taken into a glovebox.

Electrochemical analysis (half-cells)

The synthesized nanostructured NCA powders were cast into slurries on a carbon coated aluminum current collector with the composition of: 90 wt% active material, 3 wt% multi-walled carbon nanotubes, 4 wt% carbon nanofibers, and 3 wt% P3HT as a binder in *o*-xylenes (15 wt% solution). The slurries for the nanostructured NCA were assembled in a glovebox to minimize exposure to CO_2 and water. After casting the slurries with a doctor blade, the slurries were heated on a hotplate for 5 hours before being placed under vacuum in the antechamber of the glovebox to dry further overnight. For slurries made with a PVDF binder, the same procedure was followed except 2.5 wt% of PVDF in NMP was used instead of P3HT in *o*-xylenes. Electrodes 0.7 cm^2 were punched out of the slurries in the glovebox. Electrodes surrounding the cycled electrodes, which were kept completely air-free, were taken out of the glovebox and weighed on a microbalance to give an average mass loading and to calculate error bars for the cycled electrodes. The commercial bulk NCA slurries were cast in ambient air using the same material compositions, and the slurries were then dried in a vacuum oven at 120 °C overnight. Active material mass loadings ranged from 1.2–1.9 mg cm^{-2} for all NCA half-cell electrodes. The half-cell electrodes were tested in CR2032 coin cells against a Li counter electrode, with a Celgard 2400 separator and 1 M $LiPF_6$ in 1 : 1 : 1 ethylene carbonate : dimethyl carbonate : diethyl carbonate (EC : DMC : DEC). The coin cells were cycled galvanostatically from 2.7–4.2 V (*vs.* Li/Li^+) at various C-rates on an Arbin Instruments BT2000 battery testing system. Cyclic voltammetry was performed using a BioLogic VSP potentiostat/galvanostat from 2.7–4.2 V at different scan rates. Additionally, galvanostatic intermittent titration technique (GITT) measurements were performed using a Biologic VMP potentiostat/galvanostat. A minimum of 10 charge–discharge cycles were performed at various C-rates prior to the pulse-rest GITT protocol. During the GITT experiment, a C/10 constant-current pulse was applied for 30 minutes with a 30 min rest period between pulses. The sequence was repeated for both charge and discharge cycles and for varying composition x in $Li_{1-x}Ni_{0.80}Co_{0.15}Al_{0.05}O_2$ until the full voltage range (2.7–4.2 V) was covered. Electrochemical impedance spectroscopy (EIS) was performed on the nanostructured NCA electrodes in half-cells at open circuit voltage (OCV) using a BioLogic VSP potentiostat/galvanostat. Measurements were taken after various numbers of cycles at 10C between 2.7–4.2 V, with a frequency range of 100 mHz–300 kHz and a potential amplitude of 10 mV.

Electrochemical analysis (full-cells)

NCA slurries for full cells were cast air-free using the same methods as the previous section but with higher mass loadings (5–7 mg cm^{-2}). The NCA cathode electrode was paired with a Nb_2O_5–rGO anode electrode (5–7 mg cm^{-2}) to construct a full cell. To prepare the Nb_2O_5 electrode, 90 wt% of Nb_2O_5–rGO (Battery Streak Inc., Newbury Park, CA) was mixed with 10 wt% aqueous conductive binder to form a uniform slurry. The binder was composed of a 1 : 1 : 1 : 1 weight ratio of carbon nanofibers : Super P : SBR : CMC. The slurry was then cast on copper foil using a doctor blade, followed by vacuum drying for 12 hours. The resulting electrode tape was punched into 0.7 cm^2 electrodes. The NCA/Nb_2O_5–rGO full cells were assembled in a CR2032 coin cell using a glass fiber separator

 This journal is © The Royal Society of Chemistry 2025

Published on 15 August 2025. Downloaded on 2/6/2026 8:16:01 PM.

with 1 M $LiPF_6$ in 1 : 1 : 1 EC : DMC : DEC electrolyte. The cells were cycled galvanostatically from 1.0–2.8 V at various C-rates and at 10C for 2000 cycles on a BioLogic VMP potentiostat/galvanostat.

Results and discussion

Nanostructured NCA was synthesized using nitrate salts and PMMA colloidal templates (250 nm diameter)[75] that were stabilized in solution using the triblock copolymer, Pluronic F127. The homogeneous salt and polymer solution was dried and then heated using a two-step process. First, the powder was heated to 450 °C under oxygen to remove the polymer template, leaving a nanoporous NCA precursor with a surface area of 23 ± 2 $m^2 g^{-1}$ and 28 ± 5% porosity (Fig. S1). Next, the precursor was calcined at higher temperatures under oxygen to obtain the desired NCA crystal structure. Additional synthetic details can be found in the SI.

The particle size of nanostructured NCA was controlled by modifying the calcination method. A conventional heat treatment (2 hours at 800 °C under oxygen) resulted in medium sized particles (~300 nm); referred to as PMMA/no-RTA (Fig. 1, Fig. S2, S4d and Table 1). In contrast, rapid thermal annealing (RTA), where the sample is placed into a hot furnace (850 °C) for only 5 minutes, resulted in small sized particles (~150 nm) (Fig. S3a and S4b). With this short heating, considerable cation mixing remained, as evidenced by the low $I(003)/I(104)$ ratio (Fig. S3c). To produce more crystalline materials, an additional 12 hour hold at 700 °C was applied, and this two-step heating is referred to as PMMA/RTA (Fig. 1, Fig. S3b and Table 1). The additional hold allowed for short-range ordering of the cations and decreased cation mixing without significant particle size growth. However, heating at these high temperatures in both PMMA/no-RTA and PMMA/RTA led to a decrease in surface area, near the lower detection limit of nitrogen porosimetry (Fig. S5). The data also indicate that the pore sizes for all samples were large and dominantly outside the range that can be effectively measured using nitrogen porosimetry. However, for the nanostructured samples, we observed a much looser packing of the primary particles compared to the dense microsphere secondary particle structure seen in bulk materials; this should allow for greater electrolyte penetration (Fig. 1).

XRD was used to confirm the synthesis of the desired NCA crystal structure using the $I(003)/I(104)$ ratio. Both nanostructured NCAs were above the 1.2 ratio required for good electrochemical performance (Table 1 and Fig. S6). The structure was further investigated by Rietveld refinement of the XRD pattern (Fig. S6), and additional details from the refinements are shown in Table S1.[76] The refined lattice parameters can be used to calculate the slab thickness (S, TMO_6) and the interslab thickness (I, LiO_6), which is the lithium-diffusion layer thickness.[73] PMMA/no-RTA has a slightly larger interslab value (Table S1), which enables faster lithium-ion diffusion and can be a result of a lower degree of cation mixing,[72] although cation mixing is generally low for all samples.[76] The crystallite sizes determined by the refinement are smaller than what is visually observed by SEM, and this is likely due to some crystallographic disorder that further broadens the peaks.

X-ray photoelectron spectroscopy (XPS) was used to establish the oxidation state of the nickel at the surface of the NCA samples. Because of the increased sensitivity to CO_2 and water for small NCA particles, the samples were kept in a glovebox and transferred air-free for XPS analysis. Integration of the Ni

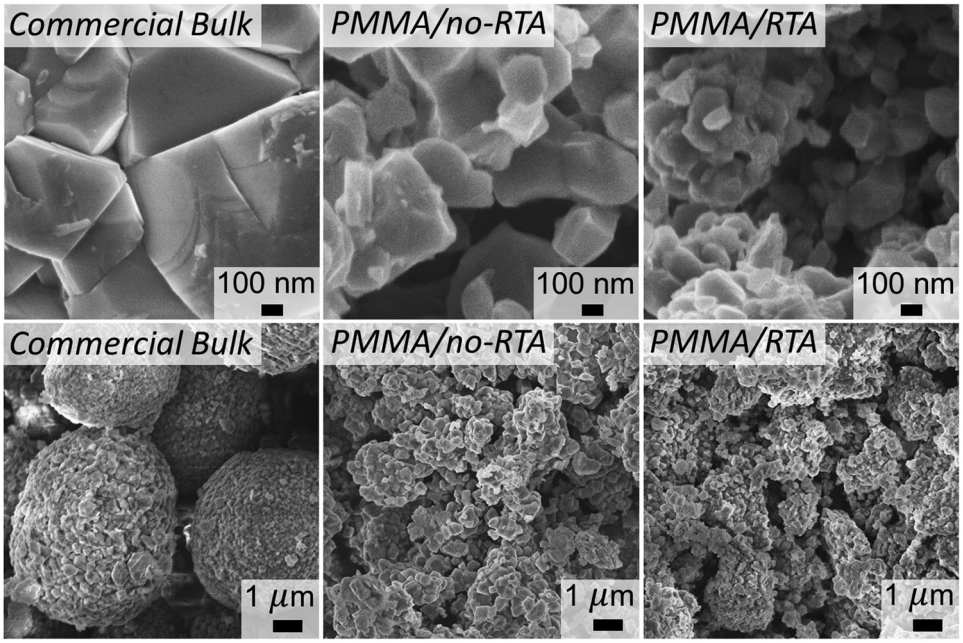

Fig. 1 High-(top) and low-(bottom) magnification SEM images of commercial bulk, PMMA/no-RTA, and PMMA/RTA NCA samples (from left to right).

Published on 15 August 2025. Downloaded on 2/6/2026 8:16:01 PM.

Table 1 $I(003)/I(104)$ ratios calculated from XRD, primary and secondary particle sizes measured from 150 particles in SEM, and air-free surface–Ni^{2+} fractions measured by XPS for the NCA materials examined here

Sample	$I(003)/I(104)$	Primary particle size measured by SEM (nm)	Secondary particle size measured by SEM (μm)	Surface–Ni^{2+} (%)
PMMA/RTA	1.23	∼150	—	67
PMMA/no-RTA	1.25	∼300	—	46
Commercial bulk	1.34	∼425	∼5–10	51

2p XPS spectra for the PMMA/RTA and PMMA/no-RTA materials can be used to calculate the surface Ni^{3+} percentage, where a higher amount of reduced nickel is attributed to the increased presence of insulating rock salt phases.[53,77–79] The PMMA/RTA samples were found to have the highest fraction of Ni^{2+} on their surface (see Table 1 for numerical results and Fig. S7 for the raw data).[80,81] We attribute this to the fact that a reducing atmosphere is formed upon thermal decomposition of PMMA.[82,83] Since PMMA/RTA was only oxidized at high temperatures for 5 minutes, this could lead to incomplete nickel oxidation.[84,85] In contrast, PMMA/no-RTA samples had the lowest Ni^{2+} fraction, which should be favorable for fast surface charge-transfer processes. The greater presence of Ni^{3+} on the surface is likely due to the longer oxidation time at a high temperature during calcination. While the fractions of Ni^{2+} measured by XPS may seem high, no impurities are seen by XRD, and the high values result because XPS is a surface sensitive measurement, probing only the first few nanometers of the sample's surface.

Ni reduction is often accompanied by Li_2CO_3 formation, so we used XPS combined with argon-ion etching to determine the relative thickness of the Li_2CO_3 layer formed on the surface of nanostructured samples kept air-free and those exposed to ambient air for 1 week (Fig. S8 and S9a). For the unetched samples, there is a greater percentage of Li_2CO_3 for the PMMA/RTA sample than the PMMA/no-RTA. Owing to the smaller size of PMMA/RTA particle sizes, the higher surface area provides more opportunity for unwanted surface reactions, including the formation of Li_2CO_3. This surface carbonate can be directly observed in TEM images, where the thickness of the surface layer is greater in the smaller sized PMMA/RTA sample than the larger PMMA/no-RTA (Fig. S4a and c). It was previously shown that for Ni-rich oxides exposed to air, at room temperature and 63% relative humidity, for 1 week led to about a 2 times increase in the amount of surface carbonates.[54] O 1s spectra were used to compare relative amounts of NCA to Li_2CO_3.[80,86] All unetched samples were covered with Li_2CO_3 (80–90%). After just 30 seconds of etching, the fraction of Li_2CO_3 decreased to ∼40% for air-free samples, but only to ∼70% for air-exposed samples. The etch rate can be roughly estimated to be 3–8 nm min^{-1} based on SiO_2.[87] However, because the Ar plasma often cannot reach the inner surfaces of porous materials, we find that some residual Li_2CO_3 always remains. Additionally, upon air exposure, the fraction of Ni^{2+} increased (Fig. S9b). From these data, we conclude that air-free samples have thinner Li_2CO_3 layers and less electrochemically inactive surface Ni^{2+}; air-free samples were thus used for electrochemical testing.

The air-free nanostructured NCA samples were cycled galvanostatically between 2.7 and 4.2 V *vs.* Li/Li^+ and compared to commercial bulk NCA at various rates from C/2 to 64C, after 3 activation cycles at C/5 (Fig. 2(a) and Fig. S10). Both NCA and P3HT have been shown to undergo degradation when cycled above 4.2 V *vs.* Li/Li^+, so to ensure stable and reversible performance, cathodes were kept below 4.2 V.[88,89] PMMA/no-RTA samples had the highest overall specific capacity, retaining 150 mAh g^{-1} at 16C and 121 mAh g^{-1} at 32C (Fig. 2(b)). PMMA/RTA, which had similar capacities to bulk NCA at slow rates, had specific capacities between those of PMMA/no-RTA and bulk NCA at 64C. The fact that both nanostructured NCAs have greater capacity than bulk at high rates indicates that the decreased lithium-ion diffusion lengths allow for faster charge/discharge kinetics. However, the smaller-sized PMMA/RTA, which should have shorter lithium-ion diffusion distances, had lower overall capacity than PMMA/no-RTA. We attribute this to the increased amount of electrochemically inactive Ni^{2+} as well as the increase in surface blocking products, such as Li_2CO_3, on the surface of the PMMA/RTA sample. Looking at the discharge capacity retention (Fig. S11) at 64C, bulk retains just 5% of its original capacity, PMMA/RTA retains 20%, and PMMA/no-RTA retains 29%. Both nanostructured NCAs showed high capacity retention of about 58% at 32C. Fig. 2(b) shows that the voltage varies linearly with capacity, consistent with both solid-solution intercalation and pseudocapacitive behavior.

For these nanoscale materials, parasitic reactions with CO_2 and water are clearly an issue. Fig. S12 shows the rate performance of electrodes prepared air-free and exposed to air. Air-exposed samples for both PMMA/no-RTA and PMMA/RTA showed lower overall capacity and poorer rate capability. Additionally, nanostructured NCA electrodes were made with a traditional PVDF binder for comparison (Fig. S12) and showed lower capacity at all rates. These data confirm that additional insulating surface layers of Li_2CO_3, NiO, or PVDF are detrimental to the fast cycling performance of nanostructured NCA.

The charge storage properties of both bulk and our nanostructured NCA materials were next studied using various kinetic analyses to better understand how nanoscale size can be used to modify diffusion limitations during charging and discharging. Most of these analyses aim to quantify the extent of pseudocapacitive behavior in a material by examining the current response in a potentiostatic measurement as a function of the rate of potential sweep. While none of the values presented below represent perfect capacitive behavior, and none of these materials are fast enough to replace electric double-layer capacitors in very high-rate applications, this exercise is still quite useful. Specifically, these analyses provide a numerical way to quantify aggregate diffusion limitations (ion diffusion, charge transfer resistance, and electrical conductivity) across a family of related materials. Because any diffusion limitation can impact overall charge/discharge kinetics, a single, aggregate value that incorporates all components is useful in comparing nanostructured materials.

We begin with an approach developed by Trasatti to quantifying capacitive and diffusion-controlled charge storage.[18,33] The base assumption of this method is that the current should

 This journal is © The Royal Society of Chemistry 2025

Published on 15 August 2025. Downloaded on 2/6/2026 8:16:01 PM.

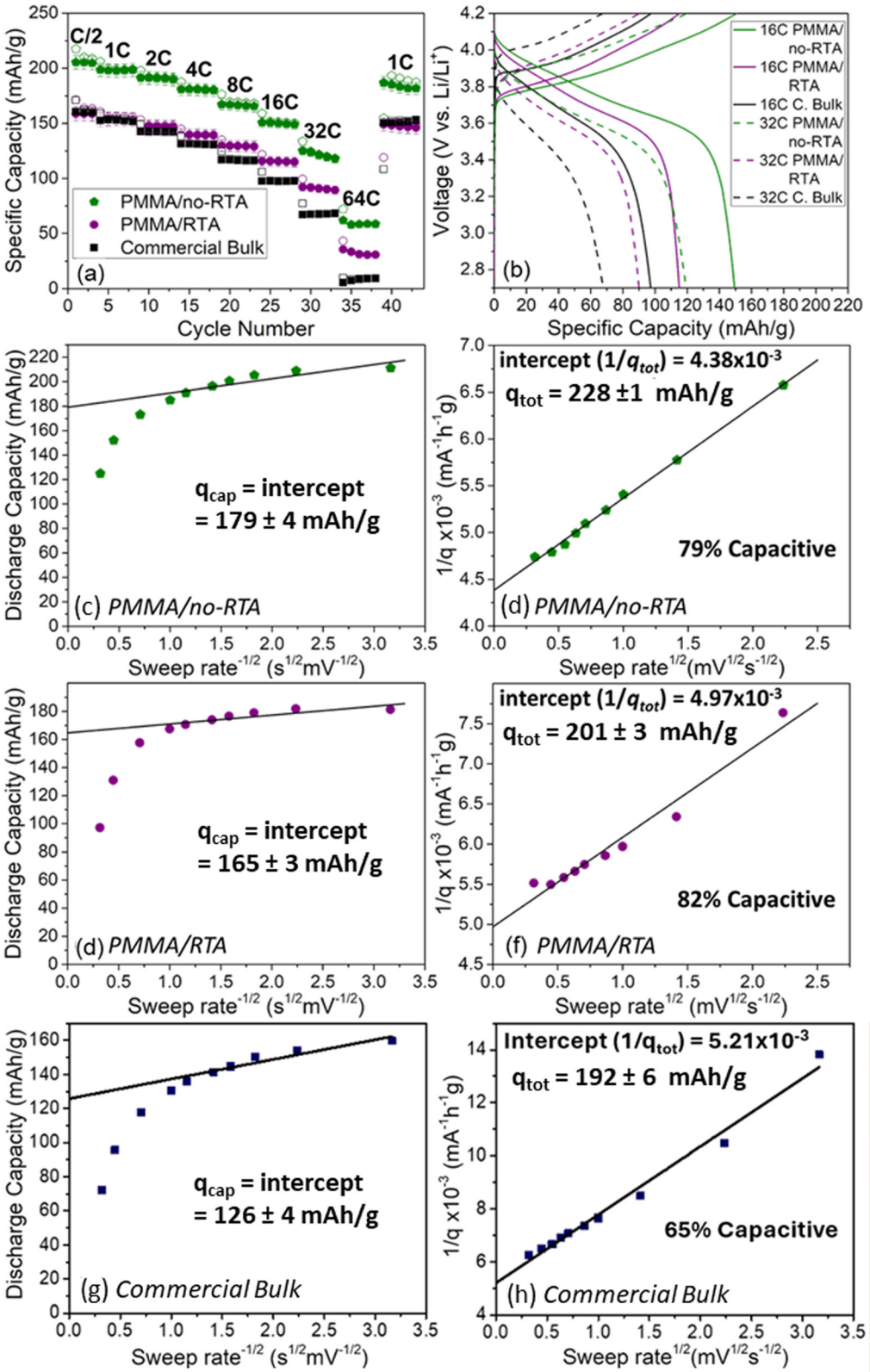

Fig. 2 (a) Specific charge (open symbols) and discharge (filled symbols) capacity from galvanostatic cycling from 2.7–4.2 V at rates from C/2 to 64C for PMMA/no-RTA (green pentagon), PMMA/RTA (purple circle), and commercial bulk NCA (black square). (b) Galvanostatic cycling curves for PMMA/no-RTA, PMMA/RTA, and commercial bulk NCA at 16C (solid line) and 32C (dashed line). (c), (e) and (g) Trasatti analysis for determination of the capacitive charge storage (q_{cap}) as the extrapolated y-intercept of the discharge capacity as a function of $v^{-1/2}$ as $v \rightarrow \infty$ for PMMA/no-RTA (c), PMMA/RTA (e), and commercial bulk (g). The q_{cap} values, with errors, are displayed on the graphs. (d), (f) and (h) Trasatti analysis for determination of the total charge storage (q_{tot}), obtained as the inverse of the extrapolated y-intercept ($1/q_{tot}$) from a plot of the inverse capacity as a function of $v^{1/2}$ as $v \rightarrow 0$ for PMMA/no-RTA (d), PMMA/RTA (f), and commercial bulk (h). The capacitive contribution for each sample is calculated as the ratio of q_{cap}/q_{tot} and displayed on the graph.

Published on 15 August 2025. Downloaded on 2/6/2026 8:16:01 PM.

vary as the square root of the voltage sweep rate (v), as predicted by classic theories of semi-infinite diffusion.[90,91] Capacitive charge storage (q_{cap}) can be extrapolated from a plot of q (voltammetric charges) *versus* $v^{-1/2}$ as $v \rightarrow \infty$, because at infinitely fast rates, diffusion-limited redox sites are excluded (Fig. 2(c), (d) and (g)). Then, the total charge storage (q_{tot}) can be extrapolated from a plot of $1/q$ *versus* $v^{1/2}$ as $v \rightarrow 0$ (long time-scale, Fig. 2(d), (f) and (h)). Using these extrapolated values, the capacitive contribution to charge storage can be calculated; by this analysis, PMMA/no-RTA and PMMA/RTA materials were 79% and 82% capacitive, respectively, while the bulk material is only 65% capacitive (Fig. 2(c)–(h)). This observation of higher capacitive fraction for the nanostructured materials in general and for PMMA/no-RTA in specific agrees well with the high-rate galvanostatic capacity retention for the three materials (Fig. 2(a) and (b)).

The next analysis builds the relationship between peak current (i) and sweep rate (v) by the following power-law equation,

$$i = av^b \tag{3}$$

where a is a constant and b can vary between 0.5 and 1, depending on whether there is a semi-infinite diffusion-controlled redox

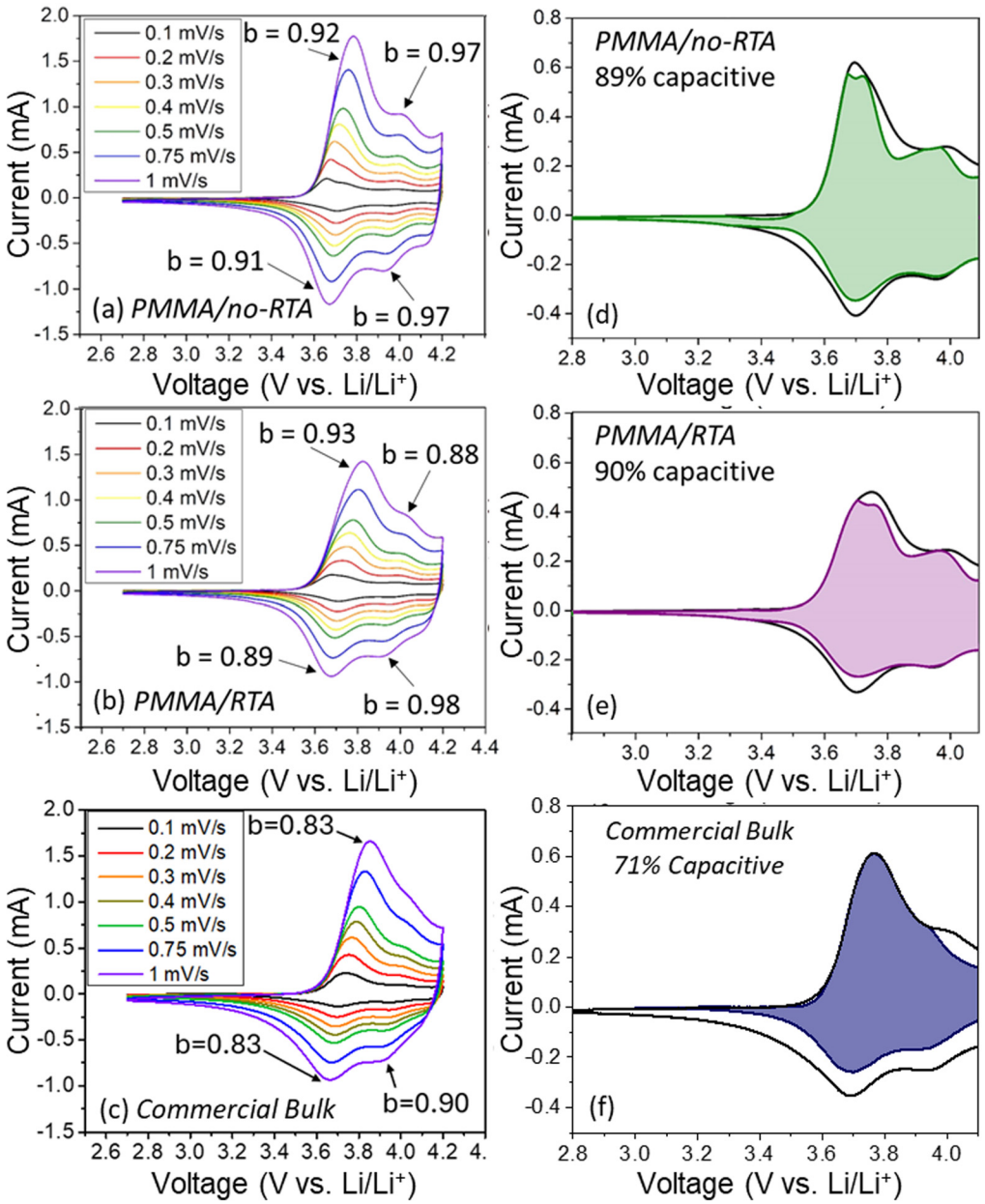

Fig. 3 (a)–(c) CV curves for PMMA/no-RTA (a), PMMA/RTA (b), and commercial bulk (c). Anodic and cathodic peaks were used to derive b-values, which are displayed on graph. The second anodic peak for the commercial bulk (f) could not be used for this analysis because the peak was not well-enough defined to accurately determine the peak current. (d)–(f) CV curves at 0.3 mV s^{-1} for PMMA/no-RTA (d, green), PMMA/RTA (b, purple), and commercial bulk (f, blue) showing the capacitive contribution as a shaded region, with the total percent capacitive contribution displayed on the graph.

 This journal is © The Royal Society of Chemistry 2025

Published on 15 August 2025. Downloaded on 2/6/2026 8:16:01 PM.

process (typical of battery materials) or a capacitive charge storage process, respectively.[26,92] The anodic and cathodic redox peaks from cyclic voltammograms (CVs) are used to derive the *b*-values (Fig. 3(a)–(c)). The average *b*-values for PMMA/no-RTA and PMMA/RTA were 0.94 and 0.92, respectively, indicating the materials are dominated by capacitor-like responses. In comparison, the average *b*-value for the bulk NCA was 0.83. Although this value is still quite high, indicating an intrinsically fast charging material, it is lower than the values obtained for the nanoscale materials.

The previous expression can also be separated into capacitor-like (k_1) and diffusion-limited (k_2) contributions to the current, each with appropriate limiting exponents.[32]

$$i = k_1\nu + k_2\nu^{1/2} \quad (4)$$

Eqn (4) allows for qualitatively resolving the capacitive contribution to charge storage over the full voltage range, which will be referred to here as k_1/k_2 analysis.[30,35] CV curves at slow sweep rates were used to determine the capacitor-like charge storage fraction, to ensure sufficient time for any slower, diffusion-controlled processes to occur. The data shows that the capacitive fraction for both PMMA/no-RTA and PMMA/RTA was in the range of 90% (Fig. 3(d) and (e)). For comparison, the bulk NCA gave a capacitive fraction of 71% (Fig. 3(f)). All of these values are in reasonable agreement with those determined by the Trasatti analysis for total charge, and indicate that the kinetics are indeed highly capacitive in the nanostructured materials, and partly capacitive in the bulk. Additionally, the peak voltage differences for both nanostructured samples are small and remain so (<0.20 V) at sweep rates up to 10 mV s^{-1} (Fig. 4(a)).[92,93] Both the kinetic results and the small difference in peak voltage are pseudocapacitive signatures.

These kinetic analyses were also performed on nanostructured NCA electrodes that were exposed to air before being assembled into a coin-cell, the results of which are summarized in Table S2. The air-exposed samples had lower average *b*-values (Fig. S13a, S14a and Table S2), meaning they are less capacitive than the air-free nanostructured NCAs. While the capacitive fraction values determined by k_1/k_E analysis are only slightly lower than what was seen for the air-free samples (Fig. S13b, S14b and Table S2), the air-exposed samples have less capacitive contribution around the redox peaks. This indicates that the non-surface redox processes are slower in these samples,[35] which is a result of the higher fractions of insulating Li_2CO_3 and NiO on their surface (Fig. S9a and b). Lastly, the Trasatti analysis indicated that the air-exposed materials had low capacitive contributions, 51% and 55% for

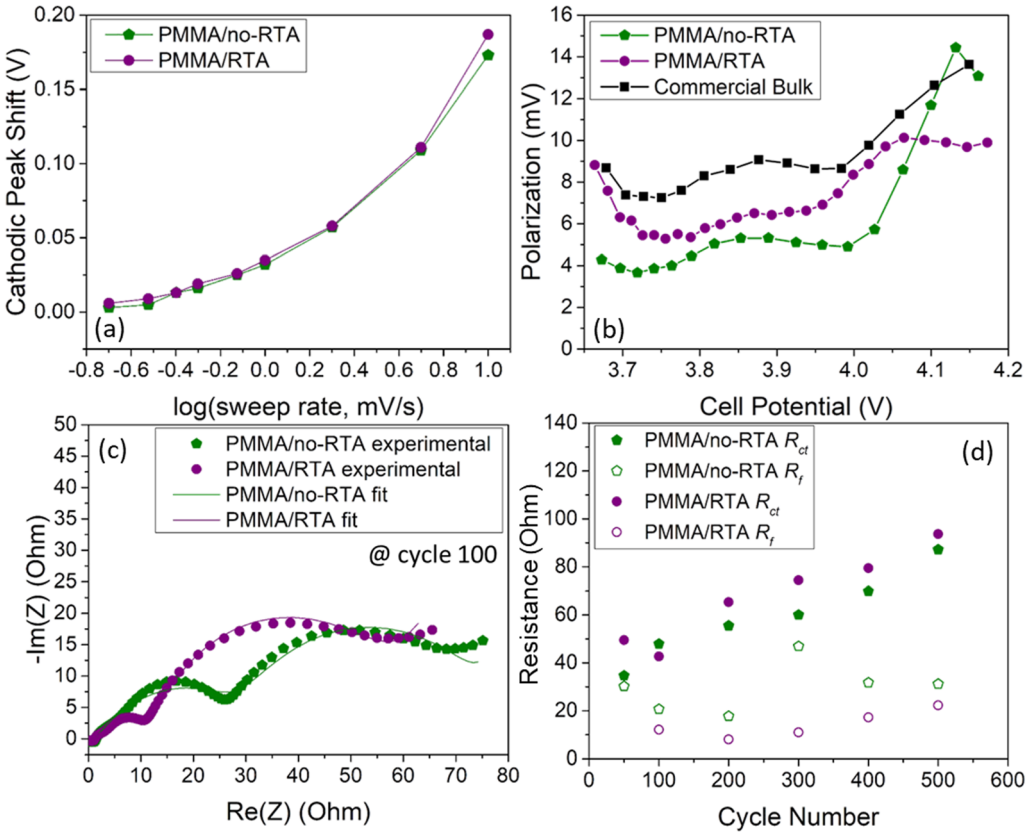

Fig. 4 (a) Cathodic peak shift for PMMA/no-RTA (green pentagon) and PMMA/RTA (purple circle). (b) Polarization *versus* cell potential obtained from GITT experiment for PMMA/no-RTA, PMMA/RTA, and commercial bulk (black square). (c) Nyquist plots of PMMA/no-RTA (green hexagon) and PMMA/RTA (purple circle, experimental data is shown by the symbol and the fit is shown by the solid line). (d) Evolution of the charge transfer resistance (R_{ct}, filled symbol) and surface film resistance (R_f, open symbol) with cycling from 50–500 cycles.

Published on 15 August 2025. Downloaded on 2/6/2026 8:16:01 PM.

air-exposed PMMA/no-RTA and PMMA/RTA, respectively (Figs. S13c, d, S14c, d, Table S2). It should be noted that nanostructured layered oxide cathodes, due to their greater surface area, have been reported to be more sensitive to air exposure than bulk materials.[94–96] This effect is evident in the reduced pseudocapacitive behavior of both the PMMA/RTA and PMMA/no-RTA materials upon exposure to air.

Additionally, nanostructured NCA electrodes with PVDF as the binder were analyzed using these kinetic methods (electrodes were kept air-free). The PVDF-binder electrodes showed similar results to air-exposed samples, in that the *b*-values and capacitive contributions from k_1/k_2 and Trasatti analyses were lower than for nanostructured NCA electrodes made air-free with P3HT as the binder (Fig. S15, S16 and Table S2). These results are as expected, since PVDF is electrically insulating and thus does not facilitate electron transport in the network. For the PVDF-binder electrodes, the separation between the first anodic and cathodic peaks was also greater than for electrodes made with P3HT (Table S2), again, because of reduced conductivity.

Next, galvanostatic intermittent titration technique (GITT) was performed in order to observe how the polarization behavior of the NCA electrodes varied with decreases in NCA particle sizes. Here, polarization is defined as the voltage change during relaxation of each GITT pulse (Fig. S17), and has contributions from ohmic, charge-transfer, and concentration polarization.[97] Polarization is then plotted *versus* cell voltage for each sample in Fig. 4(b). The data indicate that PMMA/no-RTA materials had the lowest polarization, followed by PMMA/RTA, and then bulk NCA. Diffusion coefficients were also calculated from the GITT data for the PMMA/no-RTA and PMMA/RTA materials (Fig. S18). The diffusion coefficient for the delithiation of PMMA/no-RTA is higher than that of PMMARTA across the majority of the potential range, in good agreement with the polarization data. It has been shown that an increase in NiO-like structure leads to increased polarization in NCA.[98] Although PMMA/RTA is expected to have the shortest lithium-ion diffusion lengths and thus the lowest concentration polarization, it also had the highest fraction of surface Ni^{2+}, which should increase polarization related to charge-transfer. The relative ordering of polarization across the three samples is in excellent agreement with the galvanostatic rate behavior, which shows the best rate capabilities in PMMA/no-RTA samples and the worst in the bulk NCA. These data thus demonstrate how fast cycling behavior in nanostructured materials with reactive surfaces is a balance between reducing lithium-ion diffusion distances without decreasing charge-transfer rates.

The nanostructured NCA electrodes were also investigated using electrochemical impedance spectroscopy (EIS) with cycling up to 500 cycles. Nyquist plots for PMMA/no-RTA and PMMA/RTA after 100 cycles are shown in Fig. 4(c). Both nanostructured samples display two semicircles, which have been ascribed to the resistance of lithium-ion diffusion through the cathode electrolyte interphase (CEI) surface film (R_f) and charge-transfer resistance at the interface of the NCA particle (R_{ct}), for the first and second semicircle, respectively.[65,88,99] R_{ct} slowly increases for both samples as the number of cycles increase (Fig. 4(d)), which agrees with previous literature.[65,88] The PMMA/no-RTA sample has consistently lower R_{ct}, however, which is expected because of the lower fraction of Ni^{2+} on the surface. Conversely, the PMMA/RTA sample has slightly lower R_f values, which is expected for a sample with smaller particle sizes/higher surface area.[100] R_f values for both samples remain relatively constant across cycles, suggesting a stable surface layer.[99]

Finally, to determine the viability of a fast-charging full-cell made from these materials, we paired the nanostructured PMMA/no-RTA cathode with a pseudocapacitive Nb_2O_5–rGO (reduced graphene oxide) anode at higher mass loadings (5–6 mg cm^{-2}).[101] Orthorhombic Nb_2O_5 is an excellent pseudocapacitive anode, which is often integrated with conductive carbon, such as rGO, to increase electronic conductivity.[92,102,103] The full-cell was cycled from 1.0–2.8 V at various C-rates; at 16C the full-cell retains 70% of its 1C capacity (Fig. 5(a)). Compared to a PMMA/RTA full-cell, the PMMA/no-RTA cell has higher capacity at all rates (Fig. S19). The PMMA/no-RTA full-cell was then cycled at 10C for 2000 cycles (Fig. 5(b)). The initial specific discharge capacity was 103 mAh g^{-1} normalized by the NCA active mass only. If we consider the combination of both anode and cathode masses, the resulting NCA/Nb_2O_5 cell corresponds to an energy density of 95 W h kg^{-1} at a current density of 1260 W kg^{-1}. After 2000 cycles, the discharge capacity was 74 mAh g^{-1}, a capacity retention of 72%. This capacity retention is slightly better than the capacity retention measure for bulk NCA full-cell cycled at a slower rate of 8C (Fig. S20a). The absolute capacity was significantly higher in the PMMA/no-RTA based cells than in the bulk NCA cells, however, despite the faster charge/discharge rate. The PMMA/RTA full-cells showed both lower overall capacity and lower capacity retention of only 64% after 2000 cycles at 10C (Fig. S20b). The ability of the PMMA/no-RTA full-cells to charge quickly over many cycles, without excessive capacity fade, and to show similar capacity retention to commercial bulk NCA cells indicates the promise of this nanostructured material for commercialization.

Conclusions

In this work, nanostructured NCA materials with decreased particle sizes and thus shortened lithium-ion diffusion lengths were synthesized. The nanostructured NCA materials showed pseudocapacitive signatures in both size ranges. However, because NCA has a highly reactive surface, the smallest sized NCA materials form more insulating surface layers that contain reduced Ni, as well as Li_2CO_3. These surface effects, together with increased cation disorder in the smallest grain size material, result in decreased fast-charging performance. The PMMA/no-RTA NCA, with medium sized particles and low amounts of surface Li_2CO_3/NiO, shows the best compromise of reduced diffusion lengths and low surface limitations. As a result, this medium sized material achieved the highest capacity at fast rates, showing 150 mAh g^{-1} capacity at 16C and 59 mAh g^{-1} capacity at 64C. Pseudocapacitive behavior is often associated only with very small grain-size electrode materials because those very small sizes are usually required to suppress

 This journal is © The Royal Society of Chemistry 2025

Published on 15 August 2025. Downloaded on 2/6/2026 8:16:01 PM.

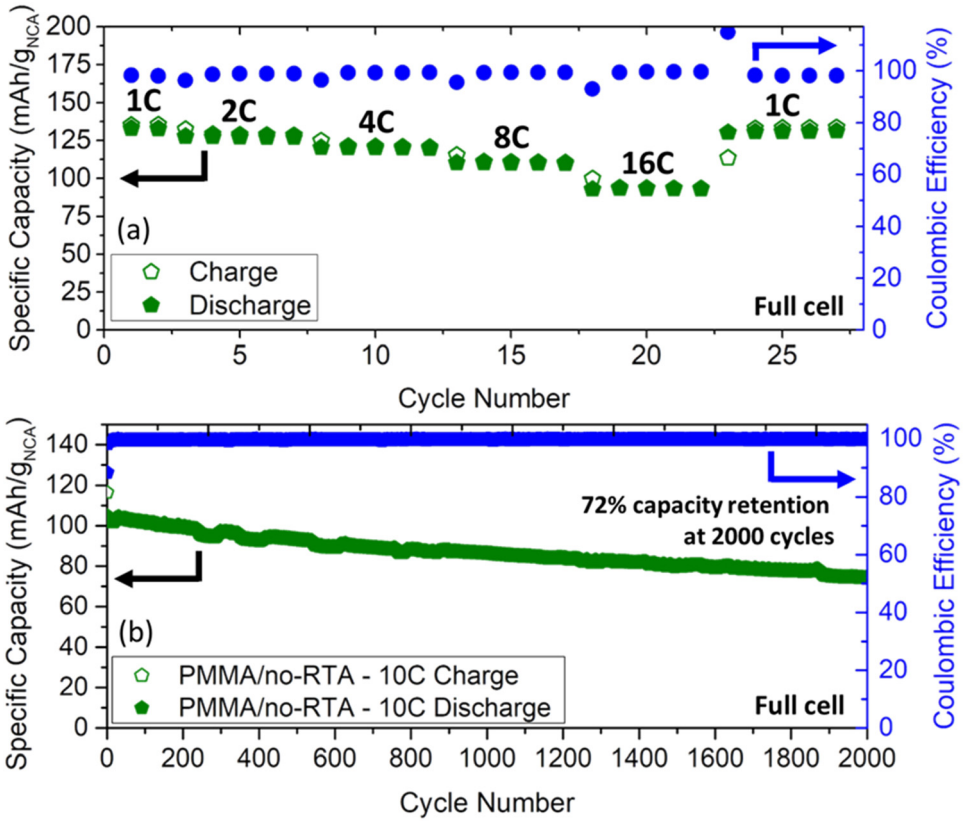

Fig. 5 Full-cell pseudocapacitor made with a PMMA/no-RTA NCA cathode and a Nb_2O_5–rGO anode cycled galvanostatically at various C-rates (a) and long-term cycling at 10C from 1.0–2.8 V (b). We observe 72% capacity retention after 2000 cycles. Specific capacity for charge is shown with open symbols, discharge with closed symbols, and the coulombic efficiency is shown in blue.

insertion-driven phase transitions. However, phase transitions in bulk NCA are suppressed by solid-solution formation, so particle sizes do not need to be extremely small in order for the material to exhibit pseudocapacitance characteristics. Indeed, the best balance between diffusion limitations and charge-transfer resistance appears not to be at the absolute smallest sized grains. We note that if smaller NCA particle sizes with ideal crystal structures and stable surfaces could be produced, then more capacitive behavior would be expected, but this goal is synthetically challenging due to the reactivity and propensity for disorder in NCA-based materials. As demonstrated in full-cell tests, nanostructured NCA shows real promise for future fast-charging applications.

Conflicts of interest

At the time of this research, S. H. Tolbert and C.-H. Lai had a financial interest in Battery Streak, Inc.

Data availability

The data supporting this article have been included as part of the SI. The SI contains additional characterization of precursor materials and materials synthesized using different temperature profiles, particle grain size distributions, and particle porosity. SI characterization data also includes high resolution TEM images, fully refined diffraction patterns, and XPS surface characterization for both air free and air exposed samples. Electrochemical data in the SI includes raw galvanostatic (GV) cycling traces as a function of current density for all samples, normalized GV capacity retention, GV capacity retention and kinetic rate parameters, along with full kinetic studies (k_1/k_2, *b*-value, and Trasatti analysis) for nanostructured electrodes made using different binders for air free and air exposed samples, and representative GITT profiles and GITT derived diffusion coefficients. Finally, full-cell data includes raw GV curves and long term GV capacity retention data for bulk non-optimized nanostructured NCA electrodes. See DOI: **https://doi.org/10.1039/d5nh00290gE**.

Acknowledgements

This work was supported by the U.S. Department of Energy, Office of Science, Office of Basic Energy Sciences, under Award DE-SC0014213 (materials synthesis and all structural and electrochemical characterization) and by a grant from Battery Streak, Inc. (full-cell fabrication and testing). The authors acknowledge the use of instruments at the Electron Imaging Center for NanoMachines supported by NIH (1S10RR23057) at the California NanoSystems Institute (CNSI) at UCLA.

Published on 15 August 2025. Downloaded on 2/6/2026 8:16:01 PM.

References

1 M. Neaimeh, S. D. Salisbury, G. A. Hill, P. T. Blythe, D. R. Scoffield and J. E. Francfort, Analysing the Usage and Evidencing the Importance of Fast Chargers for the Adoption of Battery Electric Vehicles, *Energy Policy*, 2017, **108**, 474–486, DOI: 10.1016/j.enpol.2017.06.033.

2 M. Coffman, P. Bernstein and S. Wee, Electric Vehicles Revisited: A Review of Factors That Affect Adoption, *Transp. Rev.*, 2017, **37**(1), 79–93, DOI: 10.1080/01441647.2016.1217282.

3 L. L. Zhang and X. S. Zhao, Carbon-Based Materials as Supercapacitor Electrodes, *Chem. Soc. Rev.*, 2009, **38**(9), 2520–2531, DOI: 10.1039/b813846j.

4 M. Horn, J. MacLeod, M. Liu, J. Webb and N. Motta, Supercapacitors: A New Source of Power for Electric Cars?, *Econ. Anal. Policy*, 2019, **61**, 93–103, DOI: 10.1016/j.eap.2018.08.003.

5 C. Zhu, R. Lu, L. Tian and Q. Wang, The Development of an Electric Bus with Super-Capacitors as Unique Energy Storage, *IEEE Veh. Power Propuls. Conf.*, 2006, 6–10.

6 A. Manthiram, A Reflection on Lithium-Ion Battery Cathode Chemistry, *Nat. Commun.*, 2020, **11**(1), 1550, DOI: 10.1038/s41467-020-15355-0.

7 N.-Y. Park, H.-H. Ryu, G.-T. Park, T.-C. Noh and Y.-K. Sun, Optimized Ni-Rich NCMA Cathode for Electric Vehicle Batteries, *Adv. Energy Mater.*, 2021, **11**(9), 2003767, DOI: 10.1002/aenm.202003767.

8 D. B. Ravnsbæk, K. Xiang, W. Xing, O. J. Borkiewicz, K. M. Wiaderek, P. Gionet, K. W. Chapman, P. J. Chupas, M. Tang and Y. M. Chiang, Engineering the Transformation Strain in $LiMn_yFe_{1-y}PO_4$ Olivines for Ultrahigh Rate Battery Cathodes, *Nano Lett.*, 2016, **16**(4), 2375–2380, DOI: 10.1021/acs.nanolett.5b05146.

9 K. Scanlan and A. Manthiram, Revealing the Electrochemical Kinetics of Electrolytes in Nanosized LiFePO4 Electrodes, *J. Electrochem. Soc.*, 2023, **170**(10), 100515, DOI: 10.1149/1945-7111/acfc69.

10 F. Omenya, N. A. Chernova, R. Zhang, J. Fang, Y. Huang, F. Cohen, N. Dobrzynski, S. Senanayake, W. Xu and M. S. Whittingham, Why Substitution Enhances the Reactivity of $LiFePO_4$, *Chem. Mater.*, 2013, **25**(1), 85–89, DOI: 10.1021/cm303259j.

11 M. M. Khalaf, H. G. Ibrahimov, E. H. Ismailov, H. G. I. Mai Mostafa Khalaf and E. H. I. Nanostructured, Materials: Importance, Synthesis and Characterization – A Review, *Chem. J.*, 2012, **2**(3), 118–125.

12 T. Wang, O. Sel, I. Djerdj and B. Smarsly, Preparation of a Large Mesoporous CeO_2 with Crystalline Walls Using PMMA Colloidal Crystal Templates, *Colloid Polym. Sci.*, 2006, **285**, 1–9, DOI: 10.1007/s00396-006-1526-3.

13 K. Yano, V. Nandwana, N. Poudyal, C. B. Rong and J. P. Liu, Rapid Thermal Annealing of FePt Nanoparticles, *J. Appl. Phys.*, 2008, **104**(1), 013918, DOI: 10.1063/1.2953078.

14 M. Okubo, E. Hosono, J. Kim, M. Enomoto, N. Kojima, T. Kudo, H. Zhou and I. Honma, Nanosize Effect on High-Rate Li-Ion Intercalation in $LiCoO_2$ Electrode, *J. Am. Chem. Soc.*, 2007, **129**(23), 7444–7452, DOI: 10.1021/ja0681927.

15 H.-S. Kim, J. B. Cook, S. H. Tolbert and B. Dunn, The Development of Pseudocapacitive Properties in Nanosized-MoO_2, *J. Electrochem. Soc.*, 2015, **162**(5), A5083–A5090, DOI: 10.1149/2.0141505jes.

16 Y. Zhu, X. Ji, S. Cheng, Z. Y. Chern, J. Jia, L. Yang, H. Luo, J. Yu, X. Peng, J. Wang, W. Zhou and M. Liu, Fast Energy Storage in Two-Dimensional MoO_2 Enabled by Uniform Oriented Tunnels, *ACS Nano*, 2019, **13**(8), 9091–9099, DOI: 10.1021/acsnano.9b03324.

17 L. C. Yang, W. Sun, Z. W. Zhong, J. W. Liu, Q. S. Gao, R. Z. Hu and M. Zhu, Hierarchical MoO_2/N-Doped Carbon Heteronanowires with High Rate and Improved Long-Term Performance for Lithium-Ion Batteries, *J. Power Sources*, 2016, **306**, 78–84, DOI: 10.1016/j.jpowsour.2015.11.073.

18 J. B. Cook, H. S. Kim, Y. Yan, J. S. Ko, S. Robbennolt, B. Dunn and S. H. Tolbert, Mesoporous MoS_2 as a Transition Metal Dichalcogenide Exhibiting Pseudocapacitive Li and Na-Ion Charge Storage, *Adv. Energy Mater.*, 2016, **6**(9), 1–12, DOI: 10.1002/aenm.201501937.

19 S. Luo, L. Xu, J. Li, W. Yang, M. Liu and L. Ma, Facile Synthesis of MoS_2 Hierarchical Nanostructures as Electrodes for Capacitor with Enhanced Pseudocapacitive Property, *Nano*, 2020, **15**(1), 2050011, DOI: 10.1142/S1793292020500113.

20 Q. Mahmood, S. K. Park, K. D. Kwon, S. J. Chang, J. Y. Hong, G. Shen, Y. M. Jung, T. J. Park, S. W. Khang, W. S. Kim, J. Kong and H. S. Park, Transition from Diffusion-Controlled Intercalation into Extrinsically Pseudocapacitive Charge Storage of MoS_2 by Nanoscale Heterostructuring, *Adv. Energy Mater.*, 2016, **6**(1), 1501115, DOI: 10.1002/aenm.201501115.

21 Y. Yao, H. Cumberbatch, D. D. Robertson, M. A. Chin, R. Lamkin and S. H. Tolbert, On the Interplay between Size and Disorder in Suppressing Intercalation-Induced Phase Transitions in Pseudocapacitive Nanostructured MoS2, *Adv. Funct. Mater.*, 2024, **34**(50), 2304896, DOI: 10.1002/adfm.202304896.

22 J. Choi, H. Moon and S. Fleischmann, Simultaneous Control of Crystallite Size and Interlayer Spacing of MoS_2 to Achieve Pseudocapacitive Lithium Intercalation, *Electrochim. Acta*, 2024, **476**, 143774, DOI: 10.1016/j.electacta.2024.143774.

23 Y.-M. Wei, K. D. Kumar, L. Zhang and J.-F. Li, Frontiers Pseudocapacitive Materials for Energy Storage: Properties, Mechanisms, and Applications in Supercapacitors and Batteries, *Front. Chem.*, 2025, **13**, 1636683, DOI: 10.3389/fchem.2025.1636683.

24 J. Wang, J. Polleux, J. Lim and B. Dunn, Pseudocapacitive Contributions to Electrochemical Energy Storage in TiO_2 (Anatase) Nanoparticles, *J. Phys. Chem. C*, 2007, **111**(40), 14925–14931, DOI: 10.1021/jp074464w.

25 H. Luo, Y. Chen, J. Huang, Z. Chen, X. Xia, J. Li and H. Liu, 3.3 Nm-Sized TiO_2/Carbon Hybrid Spheres Endowed with Pseudocapacitance-Dominated Superhigh-Rate Li-Ion and

 This journal is © The Royal Society of Chemistry 2025

Published on 15 August 2025. Downloaded on 2/6/2026 8:16:01 PM.

Na-Ion Storage, *Nanoscale*, 2020, **12**(13), 7366–7375, DOI: 10.1039/c9nr10750a.

26 H. Lindström, S. Södergren, A. Solbrand, H. Rensmo, J. Hjelm, A. Hagfeldt and S.-E. Lindquist, Li^+ Ion Insertion in TiO_2 (Anatase). 2. Voltammetry on Nanoporous Films, *J. Phys. Chem. B*, 1997, **101**(39), 7717–7722, DOI: 10.1021/jp970490q.

27 E. B. Tetteh, D. Valavanis, E. Daviddi, X. Xu, C. Santana Santos, E. Ventosa, D. Martín-Yerga, W. Schuhmann and P. R. Unwin, Fast Li-Ion Storage and Dynamics in TiO_2 Nanoparticle Clusters Probed by Smart Scanning Electrochemical Cell Microscopy, *Angew. Chem., Int. Ed.*, 2023, **62**(9), e202214493, DOI: 10.1002/anie.202214493.

28 J. B. Cook, T. C. Lin, H. S. Kim, A. Siordia, B. S. Dunn and S. H. Tolbert, Suppression of Electrochemically Driven Phase Transitions in Nanostructured MoS_2 Pseudocapacitors Probed Using Operando X-Ray Diffraction, *ACS Nano*, 2019, **13**(2), 1223–1231, DOI: 10.1021/acsnano.8b06381.

29 G. Zhu, D. Luo, X. Chen, J. Yang and H. Zhang, Emerging Multiscale Porous Anodes toward Fast Charging Lithium-Ion Batteries, *ACS Nano*, 2023, **17**(21), 20850–20874, DOI: 10.1021/acsnano.3c07424.

30 V. Augustyn, P. Simon and B. Dunn, Pseudocapacitive Oxide Materials for High-Rate Electrochemical Energy Storage, *Energy Environ. Sci.*, 2014, **7**(5), 1597–1614, DOI: 10.1039/c3ee44164d.

31 C. Choi, D. S. Ashby, D. M. Butts, R. H. DeBlock, Q. Wei, J. Lau and B. Dunn, Achieving High Energy Density and High Power Density with Pseudocapacitive Materials, *Nat. Rev. Mater.*, 2020, **5**, 5–19, DOI: 10.1038/s41578-019-0142-z.

32 T.-C. Liu, W. G. Pell, B. E. Conway and S. L. Roberson, Behavior of Molybdenum Nitrides as Materials for Electrochemical Capacitors, *J. Electrochem. Soc.*, 1998, **145**(6), 1882–1888, DOI: 10.1149/1.1838571.

33 S. Ardizzone, G. Fregonara and S. Trasatti, "Inner" and "Outer" Active Surface of RuO_2 Electrodes, *Electrochim. Acta*, 1990, **35**(1), 263–267, DOI: 10.1016/0013-4686(90)85068-X.

34 B. E. Conway, Transition from "Supercapacitor" to "Battery" Behavior in Electrochemical Energy Storage, *J. Electrochem. Soc.*, 1991, **138**(6), 1539–1548, DOI: 10.1149/1.2085829.

35 B. K. Lesel, J. B. Cook, Y. Yan, T. C. Lin and S. H. Tolbert, Using Nanoscale Domain Size to Control Charge Storage Kinetics in Pseudocapacitive Nanoporous $LiMn_2O_4$ Powders, *ACS Energy Lett.*, 2017, **2**(10), 2293–2298, DOI: 10.1021/acsenergylett.7b00634.

36 M. Okubo, Y. Mizuno, H. Yamada, J. Kim, E. Hosono, H. Zhou, T. Kudo and I. Honma, Fast Li-Ion Insertion into Nanosized $LiMn_2O_4$ without Domain Boundaries, *ACS Nano*, 2010, **4**(2), 741–752, DOI: 10.1021/nn9012065.

37 H. Xia, Z. Luo and J. Xie, Nanostructured $LiMn_2O_4$ and Their Composites as High-Performance Cathodes for Lithium-Ion Batteries, *Prog. Nat. Sci.:Mater. Int.*, 2012, **22**(6), 572–584, DOI: 10.1016/j.pnsc.2012.11.014.

38 T. Entwistle, E. Sanchez-Perez, G. J. Murray, N. Anthonisamy and S. A. Cussen, Co-Precipitation Synthesis of Nickel-Rich Cathodes for Li-Ion Batteries, *Energy Rep.*, 2022, **8**, 67–73, DOI: 10.1016/j.egyr.2022.06.110.

39 B. Namkoong, N.-Y. Park, G.-T. Park, J.-Y. Shin, T. Beierling, C. S. Yoon and Y.-K. Sun, High-Energy Ni-Rich Cathode Materials for Long-Range and Long-Life Electric Vehicles, *Adv. Energy Mater.*, 2022, **12**(21), 2200615, DOI: 10.1002/aenm.202200615.

40 Y. Chen, S. Song, X. Zhang and Y. Liu, The Challenges, Solutions and Development of High Energy Ni-Rich NCM/NCA LiB Cathode Materials, *J. Phys. Conf. Ser.*, 2019, **1347**(1), 012012, DOI: 10.1088/1742-6596/1347/1/012012.

41 M. Jo, M. Noh, P. Oh, Y. Kim and J. Cho, A New High Power $LiNi_{0.81}Co_{0.1}Al_{0.09}O_2$ Cathode Material for Lithium-Ion Batteries, *Adv. Energy Mater.*, 2014, **4**(13), 1301583, DOI: 10.1002/aenm.201301583.

42 J. He, M. Yang, J. Wang, R. Yu and D. Wang, Ni-Rich Cathode Materials for High-Performance Li-Ion Batteries: Challenges, Progress and Perspectives, *ChemNanoMat*, 2023, **9**(7), e202300148, DOI: 10.1002/cnma.202300148.

43 X. Zhu, H. Zhan, H. Liu and Y. Zhou, Synthesis and Characterization of $LiNi_{0.95-x}Co_xAl_{0.05}O_2$ for Lithium-Ion Batteries, *Rare Met.*, 2006, **25**(4), 303–308, DOI: 10.1016/S1001-0521(06)60058-2.

44 M. Wang and A. Navrotsky, Enthalpy of Formation of $LiNiO_2$, $LiCoO_2$ and Their Solid Solution, $LiNi_{1-x}Co_xO_2$, *Solid State Ionics*, 2004, **166**(1–2), 167–173, DOI: 10.1016/j.ssi.2003.11.004.

45 N. M. Trease, I. D. Seymour, M. D. Radin, H. Liu, H. Liu, S. Hy, N. Chernova, P. Parikh, A. Devaraj, K. M. Wiaderek, P. J. Chupas, K. W. Chapman, M. S. Whittingham, Y. S. Meng, A. Van Der Van and C. P. Grey, Identifying the Distribution of Al^{3+} in $LiNi_{0.8}Co_{0.15}Al_{0.05}O_2$, *Chem. Mater.*, 2016, **28**(22), 8170–8180, DOI: 10.1021/acs.chemmater.6b02797.

46 M. Akhilash, P. S. Salini, B. John and T. D. Mercy, A Journey through Layered Cathode Materials for Lithium Ion Cells – From Lithium Cobalt Oxide to Lithium-Rich Transition Metal Oxides, *J. Alloys Compd.*, 2021, **869**, 159239, DOI: 10.1016/j.jallcom.2021.159239.

47 C. Xu, P. J. Reeves, Q. Jacquet and C. P. Grey, Phase Behavior during Electrochemical Cycling of Ni-Rich Cathode Materials for Li-Ion Batteries, *Adv. Energy Mater.*, 2021, **11**(7), 2003404, DOI: 10.1002/aenm.202003404.

48 R. A. Yuwono, F.-M. Wang, N.-L. Wu, Y.-C. Chen, H. Chen, J.-M. Chen, S.-C. Haw, J.-F. Lee, R.-K. Xie, H.-S. Sheu, P.-Y. Chang, C. Khotimah, L. Merinda and R. Hsing, Evaluation of $LiNiO_2$ with Minimal Cation Mixing as a Cathode for Li-Ion Batteries, *Chem. Eng. J.*, 2023, **456**, 141065, DOI: 10.1016/j.cej.2022.141065.

49 W. Liu, P. Oh, X. Liu, M. J. Lee, W. Cho, S. Chae, Y. Kim and J. Cho, Nickel-Rich Layered Lithium Transition-Metal Oxide for High-Energy Lithium-Ion Batteries, *Angew. Chem., Int. Ed.*, 2015, **54**(15), 4440–4457, DOI: 10.1002/anie.201409262.

50 C. Delmas, J. P. Pérès, A. Rougier, A. Demourgues, F. Weill, A. V. Chadwick, M. Broussely, F. Perton, Ph Biensan and P. Willmann, On the Behavior of the Li_xNiO_2 System: An Electrochemical and Structural Overview, *J. Power Sources*, 1997, **68**(1), 120–125, DOI: 10.1016/S0378-7753(97)02664-5.

Published on 15 August 2025. Downloaded on 2/6/2026 8:16:01 PM.

51 T. Ohzuku, A. Ueda and M. Nagayama, Electrochemistry and Structural Chemistry of $LiNiO_2$ (*R*3*m*) for 4 Volt Secondary Lithium Cells, *J. Electrochem. Soc.*, 1993, **140**(7), 1862–1870, DOI: 10.1149/1.2220730.

52 T. Ohzuku, A. Ueda, M. Nagayama, Y. Iwakoshi and H. Komori, Comparative Study of $LiCoO_2$, $LiNi_{1/2}Co_{1/2}O_2$ and $LiNiO_2$ for 4 Volt Secondary Lithium Cells, *Electrochim. Acta*, 1993, **38**(9), 1159–1167, DOI: 10.1016/0013-4686(93)80046-3.

53 D.-H. Cho, C.-H. Jo, W. Cho, Y.-J. Kim, H. Yashiro, Y.-K. Sun and S.-T. Myung, Effect of Residual Lithium Compounds on Layer Ni-Rich $Li[Ni_{0.7}Mn_{0.3}]O_2$, *J. Electrochem. Soc.*, 2014, **161**(6), A920–A926, DOI: 10.1149/2.042406jes.

54 L. Zhang, E. A. Müller Gubler, C.-W. Tai, Ł. Kondracki, H. Sommer, P. Novák, M. El Kazzi and S. Trabesinger, Elucidating the Humidity-Induced Degradation of Ni-Rich Layered Cathodes for Li-Ion Batteries, *ACS Appl. Mater. Interfaces*, 2022, **14**(11), 13240–13249, DOI: 10.1021/acsami.1c23128.

55 H. Zhang, B. M. May, J. Serrano-Sevillano, M. Casas-Cabanas, J. Cabana, C. Wang and G. Zhou, Facet-Dependent Rock-Salt Reconstruction on the Surface of Layered Oxide Cathodes, *Chem. Mater.*, 2018, **30**(3), 692–699, DOI: 10.1021/acs.chemmater.7b03901.

56 H. Liu, Y. Yang and J. Zhang, Investigation and Improvement on the Storage Property of $LiNi_{0.8}Co_{0.2}O_2$ as a Cathode Material for Lithium-Ion Batteries, *J. Power Sources*, 2006, **162**(1), 644–650, DOI: 10.1016/j.jpowsour.2006.07.028.

57 A. Laurita, L. Zhu, P.-E. Cabelguen, J. Auvergniot, J. Hamon, D. Guyomard, N. Dupré and P. Moreau, Pristine Surface of Ni-Rich Layered Transition Metal Oxides as a Premise of Surface Reactivity, *ACS Appl. Mater. Interfaces*, 2022, **14**(37), 41945–41956, DOI: 10.1021/acsami.2c09358.

58 C.-H. Lai, D. S. Ashby, T. C. Lin, J. Lau, A. Dawson, S. H. Tolbert and B. S. Dunn, Application of Poly(3-Hexylthiophene-2,5-Diyl) as a Protective Coating for High Rate Cathode Materials, *Chem. Mater.*, 2018, **30**(8), 2589–2599, DOI: 10.1021/acs.chemmater.7b05116.

59 J. M. Kim, H. S. Park, J. H. Park, T. H. Kim, H. K. Song and S. Y. Lee, Conducting Polymer-Skinned Electroactive Materials of Lithium-Ion Batteries: Ready for Monocomponent Electrodes without Additional Binders and Conductive Agents, *ACS Appl. Mater. Interfaces*, 2014, **6**(15), 12789–12797, DOI: 10.1021/am502736m.

60 Y. Huang and J. B. Goodenough, High-Rate $LiFePO_4$ Lithium Rechargeable Battery Promoted by Electrochemically Active Polymers, *Chem. Mater.*, 2008, **20**(23), 7237–7241, DOI: 10.1021/cm8012304.

61 P. R. Berger and M. Kim, Polymer Solar Cells: P3HT:PCBM and Beyond, *J. Renewable Sustainable Energy*, 2018, **10**(1), 013508, DOI: 10.1063/1.5012992.

62 M. Jiang, Q. Zhang, X. Wu, Z. Chen, D. L. Danilov, R.-A. Eichel and P. H. L. Notten, Synthesis of Ni-Rich Layered-Oxide Nanomaterials with Enhanced Li-Ion Diffusion Pathways as High-Rate Cathodes for Li-Ion Batteries, *ACS Appl. Energy Mater.*, 2020, **3**(7), 6583–6590, DOI: 10.1021/acsaem.0c00765.

63 S. Mitra and C. Sudakar, High Rate Capability and Cyclic Stability of Ni-Rich Layered Oxide $LiNi_{0.83}Co_{0.12}Mn_{0.05-x}Al_xO_2$ Cathodes: Nanofiber versus Nanoparticle Morphology, *Battery Energy*, 2024, **3**(3), 20230066, DOI: 10.1002/bte2.20230066.

64 F. Guo, Z. Hu, Y. Xie and F. Wang, Nanostructured $LiNi_{0.8}Co_{0.1}Mn_{0.1}O_2$ with a Hollow Morphology Boosting Cycling Stability as Cathode Materials for Lithium-Ion Batteries, *ACS Appl. Nano Mater.*, 2024, **7**(13), 15215–15222, DOI: 10.1021/acsanm.4c01979.

65 Y. Chen, P. Li, S. Zhao, Y. Zhuang, S. Zhao, Q. Zhou and J. Zheng, Influence of Integrated Microstructure on the Performance of $LiNi_{0.8}Co_{0.15}Al_{0.05}O_2$ as a Cathodic Material for Lithium Ion Batteries, *RSC Adv.*, 2017, **7**(46), 29233–29239, DOI: 10.1039/c7ra04206j.

66 J. Kim, I. Lee, Y.-H. Kim, J. H. Bae, K. Hwang, H. Kang, J.-H. Shim, J.-S. Kim, C. W. Park, Y.-M. Kim and S. Yoon, Ni-Rich Cathode Material with Isolated Porous Layer Hindering Crack Propagation under 4.5 V High Cut-off Voltage Cycling, *Chem. Eng. J.*, 2022, **455**, 140578, DOI: 10.1016/j.cej.2022.140578.

67 Z. Chen, W. Zhang and Z. Yang, A Review on Cathode Materials for Advanced Lithium Ion Batteries: Microstructure Designs and Performance Regulations, *Nanotechnology*, 2019, **31**(1), 012001, DOI: 10.1088/1361-6528/ab4447.

68 R. Asakura, P. Novák and R. Robert, Colloidal Synthesis and Electrochemistry of Surface Coated Nano-$LiNi_{0.80}Co_{0.15}Al_{0.05}O_2$, *J. Electrochem. Soc.*, 2017, **164**(12), A2617–A2624, DOI: 10.1149/2.1431712jes.

69 Q. Wang, L. Zhang, P. Zhao and Z. Du, Facile Synthesis of a High-Capacity $LiNi_{0.8}Co_{0.15}Al_{0.05}O_2$ Nanoplate Cathode with a {010} Orientation for Lithium-Ion Batteries, *Int. J. Electrochem. Sci.*, 2018, **13**(11), 10382–10389, DOI: 10.20964/2018.11.15.

70 Z. Wang, H. Liu, J. Wu, W. M. Lau, J. Mei, H. Liu and G. Liu, Hierarchical $LiNi_{0.8}Co_{0.15}Al_{0.05}O_2$ Plates with Exposed {010} Active Planes as a High Performance Cathode Material for Li-Ion Batteries, *RSC Adv.*, 2016, **6**(38), 32365–32369, DOI: 10.1039/c6ra02694j.

71 Y. Wu, T. Cao, R. Wang, F. Meng, J. Zhang and C. Cao, A General Strategy for the Synthesis of Two-Dimensional Holey Nanosheets as Cathodes for Superior Energy Storage, *J. Mater. Chem. A*, 2018, **6**(18), 8374–8381, DOI: 10.1039/c8ta02327a.

72 M. Guilmard, C. Pouillerie, L. Croguennec and C. Delmas, Structural and Electrochemical Properties of $LiNi_{0.70}Co_{0.15}Al_{0.15}O_2$, *Solid State Ionics*, 2003, **160**(1–2), 39–50, DOI: 10.1016/S0167-2738(03)00106-1.

73 S. Sivaprakash, S. B. Majumder, S. Nieto and R. S. Katiyar, Crystal Chemistry Modification of Lithium Nickel Cobalt Oxide Cathodes for Lithium Ion Rechargeable Batteries, *J. Power Sources*, 2007, **170**(2), 433–440, DOI: 10.1016/j.jpowsour.2007.04.029.

74 G. He, Q. Pan and G. L. Rempel, Synthesis of Poly(Methyl Methacrylate) Nanosize Particles by Differential Microemulsion Polymerization, *Macromol. Rapid Commun.*, 2003, **24**(9), 585–588, DOI: 10.1002/marc.200390089.

 This journal is © The Royal Society of Chemistry 2025

Published on 15 August 2025. Downloaded on 2/6/2026 8:16:01 PM.

75 D. Zou, S. Ma, R. Guan, M. Park, L. Sun, J. J. Aklonis and R. Salovey, Model Filled Polymers. V. Synthesis of Cross-linked Monodisperse Polymethacrylate Beads, *J. Polym. Sci., Part A: Polym. Chem.*, 1992, **30**(1), 137–144, DOI: 10.1002/pola.1992.080300118.

76 H. Liu, H. Liu, S. H. Lapidus, Y. S. Meng, P. J. Chupas and K. W. Chapman, Sensitivity and Limitations of Structures from X-Ray and Neutron-Based Diffraction Analyses of Transition Metal Oxide Lithium-Battery Electrodes, *J. Electrochem. Soc.*, 2017, **164**(9), A1802–A1811, DOI: 10.1149/2.0271709jes.

77 H. Chen, H. Yuan, Z. Dai, S. Feng, M. Zheng, C. Zheng, J. Jin, M. Wu, X. Wu, J. Lu, Y. Lu and Z. Wen, Surface Gradient Ni-Rich Cathode for Li-Ion Batteries, *Adv. Mater.*, 2024, **36**(33), 2401052, DOI: 10.1002/adma.202401052.

78 F. Wu, J. Tian, Y. Su, J. Wang, C. Zhang, L. Bao, T. He, J. Li and S. Chen, Effect of Ni^{2+} Content on Lithium/Nickel Disorder for Ni-Rich Cathode Materials, *ACS Appl. Mater. Interfaces*, 2015, **7**(14), 7702–7708, DOI: 10.1021/acsami.5b00645.

79 E. D. Orlova, A. A. Savina, S. A. Abakumov, A. V. Morozov and A. M. Abakumov, Comprehensive Study of Li^{+}/Ni^{2+} Disorder in Ni-Rich NMCs Cathodes for Li-Ion Batteries, *Symmetry*, 2021, **13**(9), 1628, DOI: 10.3390/sym13091628.

80 X. Li, W. Ge, H. Wang, X. Yan, B. Deng, T. Chen and M. Qu, Enhancing Cycle Stability and Storage Property of $LiNi_{0.8}Co_{0.15}Al_{0.05}O_2$ by Using Fast Cooling Method, *Electrochimica Acta*, 2017, **227**(10), 225–234, DOI: 10.1016/j.electacta.2016.12.138.

81 H.-H. Ryu, H.-W. Lim, S. G. Lee and Y.-K. Sun, Near-Surface Reconstruction in Ni-Rich Layered Cathodes for High-Performance Lithium-Ion Batteries, *Nat. Energy*, 2024, **9**(1), 47–56, DOI: 10.1038/s41560-023-01403-8.

82 W. R. Zeng, S. F. Li and W. K. Chow, Review on Chemical Reactions of Burning Poly(Methyl Methacrylate) PMMA, *J. Fire Sci.*, 2002, **20**(5), 401–433, DOI: 10.1106/073490402031482.

83 M. Odziomek, M. Bahri, C. Boissiere, C. Sanchez, B. Lassalle-Kaiser, A. Zitolo, O. Ersen, S. Nowak, C. Tard, M. Giraud, M. Faustini and J. Peron, Aerosol Synthesis of Thermally Stable Porous Noble Metals and Alloys by Using Bi-Functional Templates, *Mater. Horiz.*, 2020, **7**(2), 541–550, DOI: 10.1039/c9mh01408j.

84 J. Li, W. Zhong, Q. Deng, Q. Zhang and C. Yang, Recent Progress in Synthesis and Surface Modification of Nickel-Rich Layered Oxide Cathode Materials for Lithium-Ion Batteries, *Int. J. Extreme Manuf.*, 2022, **4**(4), 042004, DOI: 10.1088/2631-7990/ac92ef.

85 L. Zhang, C. Zhao, X. Qin, S. Wang, L. He, K. Qian, T. Han, Z. Yang, F. Kang and B. Li, Heterogeneous Degradation in Thick Nickel-Rich Cathodes During High-Temperature Storage and Mitigation of Thermal Instability by Regulating Cationic Disordering, *Small*, 2021, **17**(34), 2102055, DOI: 10.1002/smll.202102055.

86 A. Grenier, H. Liu, K. M. Wiaderek, Z. W. Lebens-Higgins, O. J. Borkiewicz, L. F. J. Piper, P. J. Chupas and K. W. Chapman, Reaction Heterogeneity in $LiNi_{0.8}Co_{0.15}Al_{0.05}O_2$ Induced by Surface Layer, *Chem. Mater.*, 2017, **29**(17), 7345–7352, DOI: 10.1021/acs.chemmater.7b02236.

87 Y. C. Lu, A. N. Mansour, N. Yabuuchi and Y. Shao-Horn, Probing the Origin of Enhanced Stability of "$AlPO_4$" Nanoparticle Coated $LiCoO_2$ during Cycling to High Voltages: Combined XRD and XPS Studies, *Chem. Mater.*, 2009, **21**(19), 4408–4424, DOI: 10.1021/cm900862v.

88 X. Yang, J. Chen, Q. Zheng, W. Tu, L. Xing, Y. Liao, M. Xu, Q. Huang, G. Cao and W. Li, Mechanism of Cycling Degradation and Strategy to Stabilize a Nickel-Rich Cathode, *J. Mater. Chem. A*, 2018, **6**(33), 16149–16163, DOI: 10.1039/c8ta03041c.

89 R. Gonçalves, E. C. Pereira and L. F. Marchesi, The Overoxidation of Poly(3-Hexylthiophene) (P3HT) Thin Film: CV and EIS Measurements, *Int. J. Electrochem. Sci.*, 2017, **12**(3), 1983–1991, DOI: 10.20964/2017.03.44.

90 J. E. B. Randles, A Cathode Ray Polarograph. Part II.—The Current-Voltage Curves, *Trans. Faraday Soc.*, 1948, **44**, 327–338, DOI: 10.1039/TF9484400327.

91 A. Ševčík, *Collect. Czech. Chem. Commun.*, 1948, **13**, 349–377.

92 V. Augustyn, J. Come, M. A. Lowe, J. W. Kim, P.-L. Taberna, S. H. Tolbert, H. D. Abruña, P. Simon and B. Dunn, High-Rate Electrochemical Energy Storage through Li^{+} Intercalation Pseudocapacitance, *Nat. Mater.*, 2013, **12**, 518–522, DOI: 10.1038/nmat3601.

93 M. Forghani and S. W. Donne, Method Comparison for Deconvoluting Capacitive and Pseudo-Capacitive Contributions to Electrochemical Capacitor Electrode Behavior, *J. Electrochem. Soc.*, 2018, **165**, A664, DOI: 10.1149/2.0931803jes.

94 G.-T. Park, N.-Y. Park, H.-H. Ryu, H. Hohyun Sun, J.-Y. Hwang and Y.-K. Sun, Nano-Rods in Ni-Rich Layered Cathodes for Practical Batteries, *Chem. Soc. Rev.*, 2024, **53**, 11462–11518, DOI: 10.1039/D3CS01110K.

95 G.-T. Park, S.-B. Kim, J.-I. Yoon, N.-Y. Park, M.-C. Kim, S.-M. Han, D.-H. Kim, M.-S. Kim and Y.-K. Sun, Unraveling the New Role of Manganese in Nano and Microstructural Engineering of Ni-Rich Layered Cathode for Advanced Lithium-Ion Batteries. Adv, *Energy Mater*, 2024, **14**(22), 2400130, DOI: 10.1002/aenm.202400130.

96 W. Zhang, C. Yuan, J. Zhu, T. Jin, C. Shen and K. Xie, Air Instability of Ni-Rich Layered Oxides–A Roadblock to Large Scale Application, *Adv. Energy Mater.*, 2023, **13**(2), 2202993, DOI: 10.1002/aenm.202202993.

97 J.-H. Ryu, Polarization Behavior of $Li_4Ti_5O_{12}$ Negative Electrode for Lithium-Ion Batteries, *J. Electrochem. Sci. Technol.*, 2011, **2**(3), 136–142, DOI: 10.5229/jecst.2011.2.3.136.

98 Y. Makimura, T. Sasaki, T. Nonaka, Y. F. Nishimura, T. Uyama, C. Okuda, Y. Itou and Y. Takeuchi, Factors Affecting Cycling Life of $LiNi_{0.8}Co_{0.15}Al_{0.05}O_2$ for Lithium-Ion Batteries, *J. Mater. Chem. A*, 2016, **4**(21), 8350–8358, DOI: 10.1039/C6TA01251E.

99 B. C. Park, H. B. Kim, H. J. Bang, J. Prakash and Y. K. Sun, Improvement of Electrochemical Performance of $Li[Ni_{0.8}Co_{0.15}Al_{0.05}]O_2$ Cathode Materials by AlF_3 Coating at Various Temperatures., *Ind. Eng. Chem. Res.*, 2008, **47**(11), 3876–3882, DOI: 10.1021/ie0715308.

100 C. F. Chen and P. P. Mukherjee, Probing the Morphological Influence on Solid Electrolyte Interphase and Impedance

Response in Intercalation Electrodes, *Phys. Chem. Chem. Phys.*, 2015, **17**(15), 9812–9827, DOI: 10.1039/c4cp05758a.

101 C. H. Lai, D. Ashby, M. Moz, Y. Gogotsi, L. Pilon and B. Dunn, Designing Pseudocapacitance for Nb_2O_5/Carbide-Derived Carbon Electrodes and Hybrid Devices, *Langmuir*, 2017, **33**(37), 9407–9415, DOI: 10.1021/acs.langmuir.7b01110.

102 A. A. Lubimtsev, P. R. C. Kent, B. G. Sumpter and P. Ganesh, Understanding the Origin of High-Rate Intercalation Pseudocapacitance in Nb_2O_5 Crystals, *J. Mater. Chem. A*, 2013, **1**(47), 14951–14956, DOI: 10.1039/c3ta13316h.

103 S. Jiang, S. Dong, L. Wu, Z. Chen, L. Shen and X. Zhang, Pseudocapacitive T-Nb_2O_5/N-Doped Carbon Nanosheets Anode Enable High Performance Lithium-Ion Capacitors, *J. Electroanal. Chem.*, 2019, **842**, 82–88, DOI: 10.1016/j.jelechem.2019.04.042.

Published on 15 August 2025. Downloaded on 2/6/2026 8:16:01 PM.

 This journal is © The Royal Society of Chemistry 2025